



Topology optimization of nonlinear periodically microstructured materials for tailored homogenized constitutive properties

Reza Behrou^{a,*}, Maroun Abi Ghanem^a, Brianna C. Macnider^a, Vimarsh Verma^a, Ryan Alvey^a, Jinho Hong^a, Ashley F. Emery^b, Hyunsun Alicia Kim^c, Nicholas Boechler^a

^a Department of Mechanical and Aerospace Engineering, University of California San Diego, La Jolla, CA, USA

^b Department of Mechanical Engineering, University of Washington, Seattle, WA, USA

^c Department of Structural Engineering, University of California San Diego, La Jolla, CA, USA

ARTICLE INFO

Keywords:

Topology optimization
Nonlinear homogenization
Finite strain
Materials design
Periodic microstructure
Tailored constitutive properties

ABSTRACT

A topology optimization method is presented for the design of periodic microstructured materials with prescribed homogenized nonlinear constitutive properties over finite strain ranges. Building upon an existing computational homogenization method for periodic materials undergoing finite strain, generalized sensitivity equations are derived for the gradient-based topology optimization of periodic unit cells that account for the nonlinear homogenized response of the unit cell. The mechanical model assumes linear elastic isotropic materials, geometric nonlinearity at finite strain, and a quasi-static response. The optimization problem is solved by a nonlinear programming method and the sensitivities computed via the adjoint method. Several topology optimization examples are presented to evaluate the performance of the developed method. Furthermore, two-dimensional structures identified using this optimization method are additively manufactured and their uniaxial tensile strain response compared with the numerically predicted behavior. The optimization approach herein enables the design and development of lattice-like materials with prescribed nonlinear effective properties, for use in myriad potential applications, ranging from stress wave and vibration mitigation to soft robotics.

1. Introduction

The design of materials with tailored nonlinear properties is becoming increasingly important in materials sciences and engineering. This includes within the context of materials that exhibit constant properties over large deformation [1], novel wave tailoring behavior [2], multistability [3], and the ability to match the nonlinear properties of biological media [4]. Applications for these materials range from impact mitigation [5] to wearable electronics [6]. One of the ways the realization of material nonlinearities has been achieved is through the introduction of a periodic microstructure, where the structure of the repeating unit cell experiences geometric nonlinearity under finite strain [7]. However, it remains challenging to identify, a priori, what specific structure is needed to obtain a specific, desired, effective nonlinear response.

One method for designing materials with nonlinear responses is the use of topology optimization. Topology optimization is an affordable form-finding design methodology to obtain the optimized distribution of materials within a design domain [8]. Design of structures with geo-

metric nonlinearity via topology optimization has been successfully applied to a large class of structural problems such as stiffness design and compliant mechanisms [9–11]. Extensions to the design of periodic microstructured materials with nonlinear responses have also been recently reported [12–14]. However, the examples of Refs. [12–14] were obtained under simplified loading conditions, such as uniaxial tension in [13].

An alternative approach is the use of nonlinear homogenization techniques that can be integrated into the formulation of the topology optimization problem. For the case of linear homogenization techniques, this approach has been successfully used for multiscale design optimization of structures with linear responses [15]. Under the assumption of finite strain theory, nonlinear homogenization techniques [16,17] have also been successfully integrated into topology optimization algorithms [18,19]. However, these methods involved simplifying assumptions. In Ref. [18], unit strains were assumed at the microstructure level, which mitigates the ability for a single structure to match tailored nonlinear load–displacement behavior. In Ref. [19], the method was limited to longitudinal loading conditions.

* Corresponding author.

E-mail address: rbehrou@eng.ucsd.edu (R. Behrou).

This paper presents a topology optimization method for the design of periodic microstructured materials for tailored nonlinear homogenized constitutive responses over finite strain ranges. Generalized sensitivity equations are derived for the gradient-based topology optimization microstructured unit cells based on the computational homogenization method presented in Ref. [20] for materials undergoing finite strain. The formulated topology optimization problem and the derived sensitivities are generalized for both material and geometric nonlinearities, considering the effects of macroscopically varying local strains and/or stresses on the response of Representative Volume Element (RVE). Although the developed framework can be easily used for designing microstructures with nonlinear or anisotropic constituent materials, herein, we only focus on the design of microstructured materials for tailored homogenized constitutive properties considering isotropic linear elastic constituent materials undergoing geometric nonlinearity resulting from applied macroscale strains. The geometrically nonlinear behavior of microstructured RVE is computed using a total Lagrangian finite element formulation and the linearized forward finite element problem is solved by the arc-length method [21]. The effects of macroscale deformation and loading, i.e., applied macroscopic strain and stress, on the RVE are considered through the Periodic Boundary Conditions (PBCs). To alleviate numerical instabilities for an excessive deformation caused by low-density elements, a threshold on the elemental density, i.e., void region, is applied [22,23]. The optimization problem is solved by a nonlinear programming method using the Method of Moving Asymptotes (MMA) optimizer [24]. To interpolate material properties, the Solid Isotropic Material with Penalization (SIMP) approach [25] is used. The projection method [26] is used to regularize the optimization problem and converge to binary solutions (e.g., only one material is used in the structure, and each element is either material or void). Adjoint-based sensitivities are developed that provide the sensitivities of the nonlinear homogenized tangent stiffness tensor with respect to both state and design variables. Two-dimensional design examples and experimental calibrations are presented to study the performance of the presented approach and the response of topology optimized designs with tailored constitutive properties.

2. Physical modeling

2.1. Macro- and microscale problems

Consider macro- and microscale Boundary Value Problems (BVPs) as depicted in Fig. 1. At both macro- and microscales, the deformation, in the absence of body forces and accelerations, is governed by the balance of linear momentum:

$$\nabla_0^k \cdot \mathbf{P}^k = \mathbf{0}, \quad (1)$$

where $k \in \{M, \mu\}$ represents either the macroscopic entities, denoted with M , or the microscopic ones, denoted with μ , \mathbf{P} is the first Piola–Kirchhoff stress tensor, and ∇_0 is the gradient operator with respect to the reference configuration. For the macroscale BVP, a constitutive relationship between stress and kinematic quantities can be developed through computational homogenization techniques that numerically extract the detailed computational response of a RVE at the microscopic scale [16,17]. At any macroscopic material point, a periodically patterned RVE, given in Fig. 1b, can be considered to extract the constitutive responses through the computational homogenization [27].

2.2. Macro- and microscale kinematics

Consider the Repeating Unit Cell (RUC), given in Fig. 1c, that undergoes deformation. At both macro- and microscales, the deformation gradient, \mathbf{F} , the displacement of a material point, \mathbf{u} , and the displacement gradient, \mathbf{G} , are defined as follows:

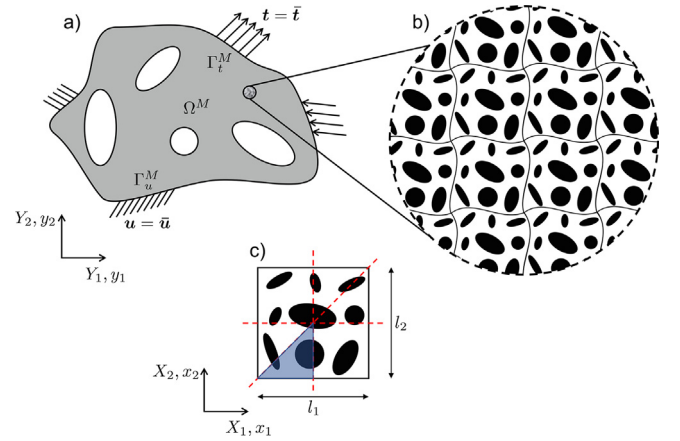


Fig. 1. a) Schematic representation of a 2D macroscale Boundary Value Problem (BVP) with a material point. Axes Y and y denote the macroscale coordinates in the reference and current configurations, and $\bar{\mathbf{u}}$ and $\bar{\mathbf{t}}$ are the prescribed displacement and traction, applied on the macroscale boundaries Γ_u^M and Γ_t^M , respectively. b) A periodically patterned microscale BVP at the material point. c) Repeating Unit Cell (RUC) at the microscale. Axes X and x denote the microscale coordinates in the reference and current configurations, respectively. The dashed lines represent the axes of symmetry and the shaded area is the design domain.

$$\mathbf{F} = \frac{\partial \mathbf{x}}{\partial \mathbf{X}}, \quad \mathbf{u} = \mathbf{x} - \mathbf{X}, \quad \mathbf{G} = \frac{\partial \mathbf{u}}{\partial \mathbf{X}} = \mathbf{F} - \mathbf{I}, \quad (2)$$

where \mathbf{I} is the second order identity tensor. Herein we follow the approach given in [20], where the deformation of the RUC is decomposed into deformations caused by the macroscopic deformation and microscopic fluctuation displacement, as depicted in Fig. 2.

For a periodically patterned RVE, the classical first-order homogenization theory can be used to relate the macroscopic deformation, \mathbf{F}^M , to the microscopic one, \mathbf{F}^μ , [28]:

$$\mathbf{F}^M = \frac{1}{|\Omega_{\text{rve}}|} \int_{\Omega_{\text{rve}}} \mathbf{F}^\mu d\Omega, \quad (3)$$

where Ω_{rve} is the volume of the RVE. A material point in the current configuration of the microscopic model, \mathbf{x} , can be related to the same material point in the reference configuration, \mathbf{X} , as follows [28,20]:

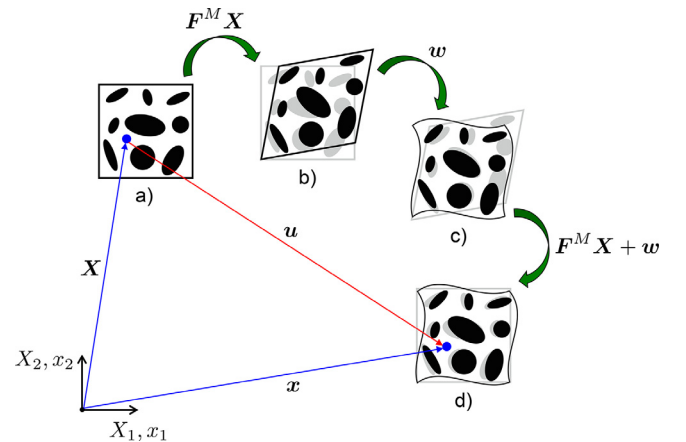


Fig. 2. Schematic representation of the deformation stages in the RUC: a) the reference configuration, b) the deformation caused by the macroscopic deformation gradient ($\mathbf{F}^M \mathbf{X}$), c) the microscopic fluctuation displacement (\mathbf{w}), and d) the current configuration.

$$\mathbf{x} = \mathbf{F}^M \mathbf{X} + \mathbf{w}, \quad (4)$$

where $\mathbf{F}^M \mathbf{X}$ indicates the macroscopic deformation, as shown in Fig. 2b. The macroscopic deformation gradient is constant over the RVE. The variable \mathbf{w} indicates the displacement caused by the microscopic fluctuation, shown in Fig. 2c.

2.3. Periodic boundary conditions

For the RVE, the relationship between the macroscopic and microscopic deformation (Eq. 3) can be simplified to the following boundary conditions [28,20]:

$$\frac{1}{|\Omega_{\text{rve}}|} \int_{\Gamma_{\text{rve}}} \mathbf{w} \cdot \mathbf{n} \, d\Gamma = 0, \quad (5)$$

where \mathbf{n} is the outgoing normal vector over the boundaries of RVE, as shown in Fig. 3. Eq. 5 indicates that the boundary conditions on the RVE must be chosen such that the contribution of the microscale fluctuation displacement, \mathbf{w} , vanishes at the boundary. This requirement can be achieved in many ways [17]. The use of PBCs is an effective way to satisfy this requirement, where imposing the corresponding points on opposite boundaries (Fig. 3) yields:

$$\mathbf{w}^+ = \mathbf{w}^-. \quad (6)$$

For the numerical implementation of Eq. 6, it is assumed that the nodal distribution on the opposite boundaries of the RVE are identical (Fig. 3). This assumption yields “a set of linearly independent boundary conditions” [20]. For two spatial dimensions and n nodes in the discretized 2D RVE, the vector form of the microscopic fluctuation displacements can be constructed using Eqs. 2 and 4 as follows:

$$\underbrace{\hat{\mathbf{w}}}_{2n \times 1} = \underbrace{\hat{\mathbf{u}}}_{2n \times 1} - \underbrace{\mathbf{T}_X}_{2n \times 4} \underbrace{\hat{\mathbf{G}}^M}_{4 \times 1}, \quad (7)$$

where $\hat{\mathbf{u}}$ is the vector of microscale nodal displacement in the RVE and $\hat{\mathbf{G}}^M$ is the vector form of the macroscale displacement gradient (with size of 4×1 for 2D and 9×1 for 3D domains). The matrix \mathbf{T}_X contains nodal coordinates of the discretized 2D RVE (see Eq. A.1 in Appendix A). Using Eq. 7, the boundary conditions given in Eq. 6 are expressed as [20]:

$$\underbrace{\mathbf{T}_p}_{2m \times 2n} \left(\underbrace{\hat{\mathbf{u}}}_{2n \times 1} - \underbrace{\mathbf{T}_X}_{2n \times 4} \underbrace{\hat{\mathbf{G}}^M}_{4 \times 1} \right) = \mathbf{0}, \quad (8)$$

where \mathbf{T}_p contains (+1) for positive nodes, (-1) for negative nodes on the boundaries, and zeros for nodes outside of the boundaries (Fig. 3).

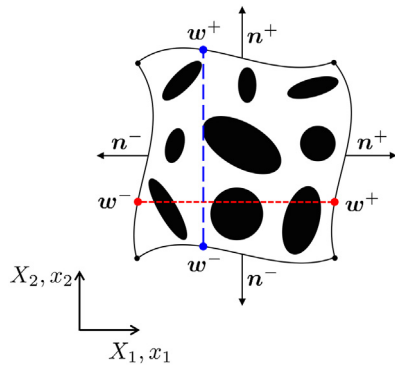


Fig. 3. Schematic representation of a 2D RVE with PBCs. w^- and w^+ correspond to microscopic fluctuation displacements on opposite boundaries, n^- and n^+ are the outgoing normal vectors on opposite boundaries.

The number of rows (i.e., $2m$) in \mathbf{T}_p denotes the number of required independent PBC equations to be solved.

For homogenization where macroscopic strains are the degrees of freedom, “it is important to avoid the rotation part of the deformation gradient, as it would lead to a singular system of equations” [20]. This can be achieved by modifying the polar decomposition of the deformation gradient tensor as follows:

$$\mathbf{F} = \mathbf{R}\mathbf{U}, \quad \text{with } \mathbf{R} = \mathbf{I}, \quad (9)$$

where \mathbf{R} is the rotation tensor and \mathbf{U} is the symmetric right stretch tensor of the decomposed deformation gradient [29], and \mathbf{I} is the identity tensor. With the assumption of $\mathbf{R} = \mathbf{I}$, the macroscale displacement gradient can be expressed as:

$$\hat{\mathbf{G}}^M = \mathbf{T}_s \hat{\mathbf{G}}_{\text{sym}}^M, \quad (10)$$

where $\hat{\mathbf{G}}_{\text{sym}}^M$ is the symmetric displacement gradient vector and \mathbf{T}_s is an adjustment matrix (with zeros and ones) that recovers the full displacement gradient vector from the components of $\hat{\mathbf{G}}_{\text{sym}}^M$. Substituting Eq. 10 into 8 leads to the following equations for PBCs that describe an implicit relationship between the microscale displacements, $\hat{\mathbf{u}}$, and the macroscale Green–Lagrange strain, $\hat{\mathbf{E}}^M$ [20]:

$$\mathbf{T}_p \left(\hat{\mathbf{u}} - \mathbf{T}_X \mathbf{T}_s \hat{\mathbf{G}}_{\text{sym}}^M \left(\hat{\mathbf{E}}^M \right) \right) = \mathbf{0}. \quad (11)$$

Additional details concerning the development of the PBCs are given in Appendix A and can be found in [20].

2.4. Microscale systems of equations

Following [20], a Lagrange multiplier approach can be used to formulate the homogenization problem:

$$\mathcal{L}(\hat{\mathbf{u}}, \hat{\boldsymbol{\lambda}}, \hat{\mathbf{E}}^M) = \mathcal{W}^M(\hat{\mathbf{u}}, \hat{\mathbf{E}}^M) - \alpha \hat{\boldsymbol{\lambda}}^T \mathbf{T}_p \left(\hat{\mathbf{u}} - \mathbf{T}_X \mathbf{T}_s \hat{\mathbf{G}}_{\text{sym}}^M \left(\hat{\mathbf{E}}^M \right) \right), \quad (12)$$

where $\hat{\boldsymbol{\lambda}}$ is a vector of Lagrange multipliers, \mathcal{W}^M is the macroscopic virtual work, and α is a positive numerical scaling factor that scales the constraint equations “for numerical conditioning of the global stiffness matrix” [20]. In this paper, we set $\alpha = E$, where E is the Young’s modulus of the base material. This would scale the constraint equations to be the same order of magnitude of the elemental stiffness matrix. The equilibrium equations for the homogenization problem are “derived from the stationary condition” [20] of Eq. 12 with respect to $\hat{\mathbf{u}}, \hat{\boldsymbol{\lambda}}, \hat{\mathbf{E}}^M$. These derivations result in the following systems of equilibrium equations:

$$\begin{aligned} \frac{\partial \mathcal{L}}{\partial \hat{\mathbf{u}}} &= \mathbf{0}, \\ \frac{\partial \mathcal{L}}{\partial \hat{\boldsymbol{\lambda}}} &= \mathbf{0}, \\ \frac{\partial \mathcal{L}}{\partial \hat{\mathbf{E}}^M} &= \mathbf{0}. \end{aligned} \quad (13)$$

The derivative of \mathcal{L} with respect to state variables (i.e., $\hat{\mathbf{u}}, \hat{\boldsymbol{\lambda}}, \hat{\mathbf{E}}^M$) leads to the following system of residual equations [20]:

$$\mathbf{r}(\hat{\mathbf{u}}, \hat{\boldsymbol{\lambda}}, \hat{\mathbf{E}}^M) = \begin{pmatrix} \frac{1}{|\Omega_{\text{rve}}|} \mathbf{f}_{\text{int}}(\hat{\mathbf{u}}) - \alpha \mathbf{T}_p^T \hat{\boldsymbol{\lambda}} \\ -\alpha \mathbf{T}_p \hat{\mathbf{u}} + \alpha \mathbf{T}_p \mathbf{T}_X \mathbf{T}_s \hat{\mathbf{G}}_{\text{sym}}^M \left(\hat{\mathbf{E}}^M \right) \\ \hat{\mathbf{S}}_{\text{int}}^M \left(\hat{\boldsymbol{\lambda}}, \hat{\mathbf{E}}^M \right) \end{pmatrix} - \begin{pmatrix} \mathbf{0} \\ \mathbf{0} \\ \hat{\mathbf{S}}^M \end{pmatrix}, \quad (14)$$

where \mathbf{f}_{int} is the microscopic internal force vector, $\hat{\mathbf{S}}^M$ is the macroscopic stress at a material point (i.e., applied macroscopic stress on

the RVE), and $\widehat{\mathbf{S}}_{\text{int}}^M$ is the so-called internal macroscopic stress that corresponds to the macroscopic deformation of the RVE given as follows:

$$\begin{aligned} \widehat{\mathbf{S}}_{\text{int}}^M(\widehat{\boldsymbol{\lambda}}, \widehat{\mathbf{E}}^M) &= \alpha \left(\mathbf{Z}(\widehat{\mathbf{E}}^M) \right)^T \widehat{\boldsymbol{\lambda}}, \\ \mathbf{Z} &= \mathbf{T}_p \mathbf{T}_x \mathbf{T}_s \overline{\mathbf{M}}^{-1}, \quad \text{with } \overline{\mathbf{M}} = \overline{\mathbf{I}} + \overline{\mathbf{G}}^M. \end{aligned} \quad (15)$$

The matrix $\overline{\mathbf{G}}^M$ collects the components of the symmetric displacement gradient and $\overline{\mathbf{I}}$ is a diagonal matrix [20]. Detail on $\overline{\mathbf{G}}^M$ and $\overline{\mathbf{I}}$ are given in Appendix A.

2.5. Homogenized tangent stiffness tensor

The macroscopic homogenized tangent stiffness tensor, \mathbb{C}^{eff} , can be defined through the stress–strain relationship as follows [20]:

$$\delta \widehat{\mathbf{S}}^M = \mathbb{C}^{\text{eff}} \delta \widehat{\mathbf{E}}^M. \quad (16)$$

The tensor \mathbb{C}^{eff} can be computed from the converged solution of the microscopic equilibrium equations (i.e., Eq. 14) as follows [20]:

$$\begin{aligned} \mathbb{C}^{\text{eff}}(\widehat{\boldsymbol{\lambda}}, \widehat{\mathbf{E}}^M) &= \mathbb{C}^s(\widehat{\boldsymbol{\lambda}}, \widehat{\mathbf{E}}^M) \\ &\quad - \left[\mathbf{0} \quad \alpha \mathbf{Z}^T(\widehat{\mathbf{E}}^M) \right] \underbrace{\begin{bmatrix} \frac{1}{|\Omega_{\text{rve}}|} \mathbf{K}(\widehat{\boldsymbol{\lambda}}) & -\alpha \mathbf{T}_p^T \\ -\alpha \mathbf{T}_p & \mathbf{0} \end{bmatrix}^{-1}}_{\mathbf{Y}} \begin{bmatrix} \mathbf{0} \\ \alpha \mathbf{Z}(\widehat{\mathbf{E}}^M) \end{bmatrix}, \end{aligned} \quad (17)$$

where $\mathbf{K} = \partial f_{\text{int}}^{\mu}(\widehat{\boldsymbol{\lambda}})/\partial \widehat{\boldsymbol{\lambda}}$ is the microscale tangent stiffness matrix and \mathbb{C}^s is a type of geometrical stiffness tensor given as:

$$\mathbb{C}^s = -\overline{\mathbf{M}}^{-1} \overline{\mathbf{S}}^M \overline{\mathbf{M}}^{-1}, \quad (18)$$

with $\overline{\mathbf{S}}^M$ derived from the components of $\widehat{\mathbf{S}}_{\text{int}}^M$ (defined in Eq. 15), see Appendix A.

To facilitate the complex derivations of \mathbb{C}^{eff} used for sensitivity analysis purposes, we simplified Eq. 17 by modifying the inverse of \mathbf{Y} matrix in the following setting. Consider a 2×2 block of matrices given as follows:

$$\mathbf{R} = \begin{bmatrix} \mathbf{A}_{k \times m} & \mathbf{B}_{k \times n} \\ \mathbf{C}_{l \times m} & \mathbf{D}_{l \times n} \end{bmatrix}_{(k+l) \times (m+n)}, \quad (19)$$

where \mathbf{R} is a square matrix with $k+l = m+n$. For the case when \mathbf{A} is a non-singular square matrix (i.e., $\mathbf{A}^{-1} \neq 0$ and $k = m$) and \mathbf{D} is a square matrix (i.e., $l = n$), the square matrix \mathbf{R} is invertible if and only if the Schur complement (i.e., $\mathbf{D} - \mathbf{C}\mathbf{A}^{-1}\mathbf{B}$) of \mathbf{A} is invertible [30]. For this case, the inverse of \mathbf{R} is given as follows [30]:

$$\mathbf{R}^{-1} = \begin{bmatrix} \mathbf{A}^{-1} + \mathbf{A}^{-1}\mathbf{B}(\mathbf{D} - \mathbf{C}\mathbf{A}^{-1}\mathbf{B})^{-1}\mathbf{C}\mathbf{A}^{-1} & -\mathbf{A}^{-1}\mathbf{B}(\mathbf{D} - \mathbf{C}\mathbf{A}^{-1}\mathbf{B})^{-1} \\ -(\mathbf{D} - \mathbf{C}\mathbf{A}^{-1}\mathbf{B})^{-1}\mathbf{C}\mathbf{A}^{-1} & (\mathbf{D} - \mathbf{C}\mathbf{A}^{-1}\mathbf{B})^{-1} \end{bmatrix}. \quad (20)$$

The \mathbf{Y} matrix given in Eq. 17 contains a 2×2 block of matrices where its internal matrices have the aforementioned properties with:

$$\mathbf{A} = \frac{1}{|\Omega_{\text{rve}}|} \mathbf{K}, \quad \mathbf{B} = \mathbf{C}^T = -\alpha \mathbf{T}_p^T, \quad \mathbf{D} = \mathbf{0}, \quad (21)$$

where the stiffness matrix, \mathbf{K} , is a non-singular square matrix, \mathbf{D} is a square matrix, and the Schur complement of \mathbf{A} is invertible; therefore, one can conclude that $\mathbf{Y}^{-1} = \mathbf{R}^{-1}$. The use of Eqs. 20 and 21 in 17 yields the simplified form of the homogenized stiffness tensor as follows:

$$\begin{aligned} \mathbb{C}^{\text{eff}} &= \mathbb{C}^s - \mathbf{Z}^T \mathbf{\Psi}^{-1} \mathbf{Z}, \quad \text{with} \\ \mathbf{\Psi} &= -|\Omega_{\text{rve}}| \mathbf{T}_p \mathbf{K}^{-1} \mathbf{T}_p^T. \end{aligned} \quad (22)$$

3. Sensitivity analysis

3.1. Adjoint sensitivity

Adjoint-based sensitivities are derived to compute the sensitivity of a criterion (the objective or a constraint) with respect to a design-dependent fictitious elemental density, ρ^e , as follows:

$$\frac{d\mathcal{Z}}{d\rho^e} = \frac{\partial \mathcal{Z}}{\partial \rho^e} + \tilde{\boldsymbol{\chi}}^T \frac{\partial \mathbf{r}}{\partial \rho^e}, \quad (23)$$

where \mathcal{Z} is defined as the objective function or a constraint, and $\tilde{\boldsymbol{\chi}}$ is the vector of adjoint solutions, computed as follows:

$$\left(\frac{\partial \mathbf{r}}{\partial \mathbf{s}} \right)^T \tilde{\boldsymbol{\chi}} = - \left(\frac{\partial \mathcal{Z}}{\partial \mathbf{s}} \right)^T, \quad (24)$$

where $\mathbf{s} = [\widehat{\boldsymbol{\lambda}}, \widehat{\mathbf{E}}^M]^T$ is the vector of state variables satisfying the microscale equilibrium. The derivatives of the residuals with respect to state variables are computed using Eq. 14. For a generalized optimization problem, a criterion could be an explicit function of the homogenized tangent stiffness tensor, \mathbb{C}^{eff} . Hence, the detail on the derivation of \mathbb{C}^{eff} with respect to the design and state variables are given below.

3.2. Derivative of \mathbb{C}^{eff} with respect to the elemental density

The partial derivative of \mathbb{C}^{eff} with respect to ρ^e are derived from Eq. 22 as follows:

$$\frac{\partial \mathbb{C}^{\text{eff}}}{\partial \rho^e} = \mathbf{Z}^T \mathbf{\Psi}^{-1} \frac{\partial \mathbf{\Psi}}{\partial \rho^e} \mathbf{\Psi}^{-1} \mathbf{Z}, \quad \text{with } \frac{\partial \mathbf{\Psi}}{\partial \rho^e} = |\Omega_{\text{rve}}| \mathbf{T}_p \mathbf{K}^{-1} \frac{\partial \mathbf{K}}{\partial \rho^e} \mathbf{K}^{-1} \mathbf{T}_p^T. \quad (25)$$

We note that \mathbb{C}^s and \mathbf{Z} (in Eq. 22) are independent of ρ^e . The term $\partial \mathbf{K}/\partial \rho^e$ can be computed from the material interpolation scheme given in Section 4.2.

3.3. Derivative of \mathbb{C}^{eff} with respect to microscale displacements

From Eq. 22, the partial derivative of \mathbb{C}^{eff} with respect to a displacement Degree-Of-Freedom (DOF), \widehat{u}_p , is given as follows:

$$\begin{aligned} \frac{\partial \mathbb{C}^{\text{eff}}}{\partial \widehat{u}_p} &= \mathbf{Z}^T \mathbf{\Psi}^{-1} \frac{\partial \mathbf{\Psi}}{\partial \widehat{u}_p} \mathbf{\Psi}^{-1} \mathbf{Z}, \quad \text{with} \\ \frac{\partial \mathbf{\Psi}}{\partial \widehat{u}_p} &= |\Omega_{\text{rve}}| \mathbf{T}_p \mathbf{K}^{-1} \frac{\partial \mathbf{K}}{\partial \widehat{u}_p} \mathbf{K}^{-1} \mathbf{T}_p^T. \end{aligned} \quad (26)$$

The detail on the first and second derivatives of the microscale internal strain energy is given in Appendix B. The derivations consider both material and geometric nonlinearities.

3.4. Derivative of \mathbb{C}^{eff} with respect to Lagrange multipliers

The derivative of \mathbb{C}^{eff} (i.e., Eq. 22) with respect to a Lagrange multiplier DOF, $\widehat{\lambda}_r$, is given as:

$$\frac{\partial \mathbb{C}^{\text{eff}}}{\partial \widehat{\lambda}_r} = -\overline{\mathbf{M}}^{-1} \frac{\partial \overline{\mathbf{S}}^M}{\partial \widehat{\lambda}_r} \frac{\partial \widehat{\mathbf{S}}_{\text{int}}^M}{\partial \widehat{\lambda}_r} \overline{\mathbf{M}}^{-1}. \quad (27)$$

The term $\partial \widehat{\mathbf{S}}_{\text{int}}^M / \partial \widehat{\lambda}_r$ can be computed from Eq. 15 and the derivatives of $\overline{\mathbf{S}}^M$ with respect to internal stress components can be computed from Eq. A.6.

3.5. Derivative of \mathbb{C}^{eff} with respect to macroscale strains

The derivative of \mathbb{C}^{eff} with respect to a macroscale strain DOF, \widehat{E}_r^M , can be computed from Eq. 22 as follows:

$$\frac{\partial \mathbb{C}^{\text{eff}}}{\partial \widehat{E}_r^M} = \frac{\partial \mathbb{C}^s}{\partial \widehat{E}_r^M} - \left(\frac{\partial \mathbf{Z}^T}{\partial \widehat{E}_r^M} \mathbf{\Psi}^{-1} \mathbf{Z} + \mathbf{Z}^T \mathbf{\Psi}^{-1} \frac{\partial \mathbf{Z}}{\partial \widehat{E}_r^M} \right), \quad (28)$$

where the derivative of \mathbb{C}^s and \mathbf{Z} with respect to macroscale strain DOFs are computed from Eqs. 15 and 18 as follows:

$$\begin{aligned} \frac{\partial \mathbb{C}^s}{\partial \bar{\mathbf{E}}_r^M} &= - \left(\frac{\partial \bar{\mathbf{M}}^{-1}}{\partial \bar{\mathbf{E}}_r^M} \bar{\mathbf{S}}^M \bar{\mathbf{M}}^{-1} + \bar{\mathbf{M}}^{-1} \frac{\partial \bar{\mathbf{S}}^M}{\partial \bar{\mathbf{E}}_r^M} \bar{\mathbf{M}}^{-1} + \bar{\mathbf{M}}^{-1} \bar{\mathbf{S}}^M \frac{\partial \bar{\mathbf{M}}^{-1}}{\partial \bar{\mathbf{E}}_r^M} \right), \\ \frac{\partial \mathbf{Z}}{\partial \bar{\mathbf{E}}_r^M} &= -\mathbf{Z} \frac{\partial \bar{\mathbf{G}}^M}{\partial \hat{\mathbf{G}}_{\text{sym}}^M} \bar{\mathbf{M}}^{-1} \bar{\mathbf{M}}^{-1}, \end{aligned} \quad (29)$$

with

$$\frac{\partial \bar{\mathbf{M}}^{-1}}{\partial \bar{\mathbf{E}}_r^M} = -\bar{\mathbf{M}}^{-1} \frac{\partial \bar{\mathbf{G}}^M}{\partial \hat{\mathbf{G}}_{\text{sym}}^M} \bar{\mathbf{M}}^{-1} \bar{\mathbf{M}}^{-1}. \quad (30)$$

The derivatives of $\bar{\mathbf{G}}^M$ with respect to the components of $\hat{\mathbf{G}}_{\text{sym}}^M$ can be computed from Eq. A.4.

4. Topology optimization

The optimization problem presented here is included as an example of how to consider the components of the homogenized tangent stiffness tensor, \mathbb{C}^{eff} , in the formulation of the objective function and constraints. Many combinations of individual components of the homogenized tangent stiffness tensor can be considered (for instance, to maximize the material bulk modulus [31,32] or Poisson's ratio [33]). In this paper, the objective is formulated to minimize the difference between the computed and target tangent stiffness tensors. The generalized formulation of the objective and constraints, material interpolation, and regularization are discussed below.

4.1. Objective and constraints

The optimization problem for minimizing the difference between the homogenized tangent stiffness tensor, \mathbb{C}^{eff} , and the target tangent stiffness tensor, $\mathbb{C}^{\text{target}}$, is formulated as follows:

$$\begin{aligned} \min_{\boldsymbol{\phi}} \quad & z = \sum_{i,j,k,l=1}^D \left(\mathbb{C}_{ijkl}^{\text{eff}}(s(\boldsymbol{\phi}), \boldsymbol{\phi}) - \mathbb{C}_{ijkl}^{\text{target}} \right)^2 \\ \text{subject to} \quad & \begin{cases} \mathbf{r}(s(\boldsymbol{\phi}), \boldsymbol{\phi}) = \mathbf{0} \\ \mathcal{G} = \sum_{e \in \Omega_{\text{ave}}} \rho^e(\boldsymbol{\phi}) v^e - V_{\text{max}} \leq 0 \\ 0 \leq \phi_k \leq 1 \quad \forall k = 1, \dots, N_{\phi} \end{cases} \end{aligned} \quad (31)$$

where z is the objective function, D is the spatial dimension, $\boldsymbol{\phi}$ is the vector of independent design variables, ρ^e is the fictitious elemental density, \mathcal{G} is the volume constraint, v^e is the elemental volume, and V_{max} is the prescribed volume fraction of the solid material. The Nested ANalysis and Design (NAND) approach is used to solve the microscale finite element problem where only the design variables, $\boldsymbol{\phi}$, are treated as the independent optimization variables [34]. The independent design variables are bounded with lower and upper bounds with N_{ϕ} that denotes the number of design variables.

4.2. Material interpolation

The SIMP approach [25] is used for the interpolation of material properties with an artificial power law that penalizes intermediate density values. Using this approach, the stiffness of the microstructure is related to topology through the design dependent Young's modulus as follows:

$$E^e(\rho^e) = (\rho_{\text{min}}^e + (\rho^e)^{\bar{p}} (1 - \rho_{\text{min}}^e)) E_0^e, \quad (32)$$

where E_0^e is the Young's modulus of pure solid material, $\bar{p} \geq 1$ is the SIMP exponent penalty term, and ρ_{min}^e is a small positive number to maintain positive definiteness of the global stiffness matrix. We set $\rho^e = 1$ for the solid region and $\rho^e = 0$ for the void region.

4.3. Regularization

To circumvent instabilities caused by checkerboard patterns [35], and convergence to binary solutions, numerical regularization approaches such as filtering [10] and projection [36,37,26] are commonly used in topology optimization. In this paper, we adopt the linear density filtering [10] and the threshold projection [26] approaches. Our computational experiment showed that the threshold projection approach results in a more stable convergence behavior and yields discrete designs [26,13]. To eliminate the checkerboard patterns, the independent nodal design variables field, $\boldsymbol{\phi}$, is regularized using a linear filtering scheme as follows [10]:

$$\begin{aligned} \mu^e(\boldsymbol{\phi}) &= \frac{\sum_{i \in N^h} \hat{\mathbf{W}}_i \phi_i}{\sum_{i \in N^h} \hat{\mathbf{W}}_i}, \quad \text{with} \\ \hat{\mathbf{W}}_i &= \frac{r_{\text{min}} - \|\mathbf{x}_i - \mathbf{x}^e\|}{r_{\text{min}}}, \end{aligned} \quad (33)$$

where N^h contains all design variables located within a radius r_{min} , \mathbf{x}_i and \mathbf{x}^e are the position of node i and the central position of element e , respectively. The elemental density is then related to the regularized design variables through the threshold projection where different design realizations for the manufacturing process can be considered by choosing different thresholds, η :

$$\rho^e(\boldsymbol{\phi}) = \frac{\tanh(\beta\eta) + \tanh(\beta(\mu^e(\boldsymbol{\phi}) - \eta))}{\tanh(\beta\eta) + \tanh(\beta(1 - \eta))}. \quad (34)$$

The projection parameter, $\beta > 0$, dictates the curvature of the regularization which approaches the Heaviside function as $\beta \rightarrow \infty$ [26].

Accounting for the filtering and projection (i.e., Eqs. 33), the derivative of the objective function and the residual (given in Eq. 23) with respect to an independent design variable (ϕ_k) is given through the chain rule as follows:

$$\begin{aligned} \frac{\partial \mathcal{L}}{\partial \phi_k} &= \sum_{e \in N^e} \frac{\partial \mathcal{L}}{\partial \rho^e} \frac{\partial \rho^e}{\partial \mu^e} \frac{\partial \mu^e}{\partial \phi_k}, \\ \frac{\partial \mathbf{r}}{\partial \phi_k} &= \sum_{e \in N^e} \frac{\partial \mathbf{r}}{\partial \rho^e} \frac{\partial \rho^e}{\partial \mu^e} \frac{\partial \mu^e}{\partial \phi_k}, \\ \frac{\partial \mathcal{G}}{\partial \phi_k} &= \sum_{e \in N^e} \frac{\partial \mathcal{G}}{\partial \rho^e} \frac{\partial \rho^e}{\partial \mu^e} \frac{\partial \mu^e}{\partial \phi_k}, \end{aligned} \quad (35)$$

where N^e defines the set containing all elements located within the distance r_{min} of design variables k . The second and third part of the derivation in Eq. 35 (i.e., $\frac{\partial \rho^e}{\partial \mu^e}$ and $\frac{\partial \mu^e}{\partial \phi_k}$) can be computed from Eqs. 33 and 34.

4.4. Algorithmic summary

For the design problems presented in this paper, the MMA optimizer [24] is used, which has proven an efficient and reliable gradient-based optimization engine for solving a wide range of nonlinear structural optimization problems [38]. The most relevant MMA parameters are summarized in Table 1. A flowchart describing the topology optimization procedure is given in Fig. 4. At each design iteration, the microscale nonlinear finite element problem is solved using the arc-length method [21]. We note that the arc-length method is very efficient in solving nonlinear systems of equations when the prob-

Table 1
MMA parameters used in topology optimization problems.

Description	Symbol	Value
Initial asymptote parameter	σ_{MMA}	0.017
Lower asymptote adaptivity	α_-	0.55
Upper asymptote adaptivity	α_+	1.05
Constraint penalty	c_i	1000

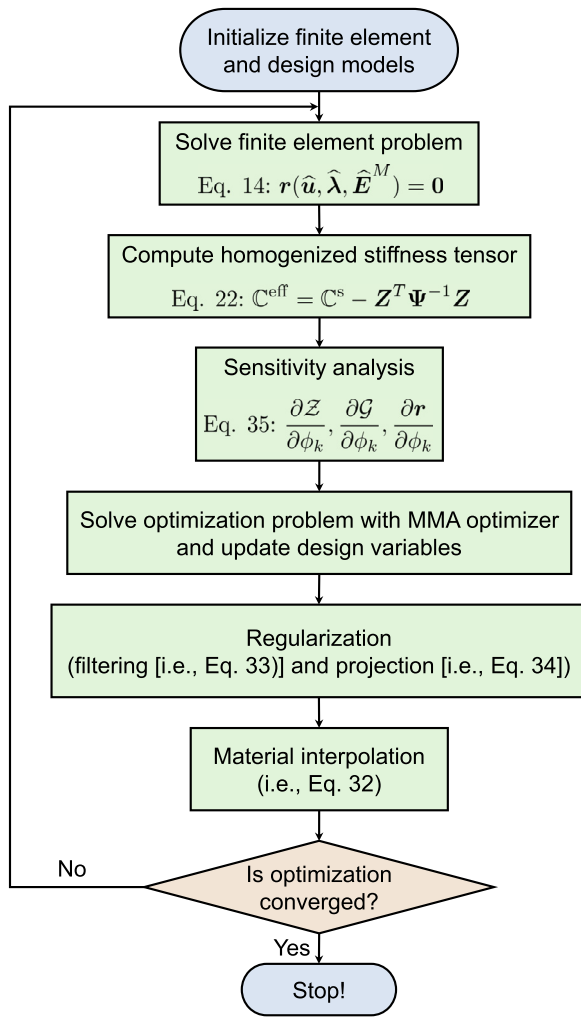


Fig. 4. The flowchart describing the topology optimization procedure.

lem under consideration exhibits one or more critical instabilities due to an increase of the external forces or a problem undergoes large deformation. The finite element problem is considered converged if the relative change of the residuals (Eq. 14) is less than 10^{-10} . The solution for the adjoint variables given in Eq. 24 is obtained using the direct linear solver with lower-upper (LU) factorization [39]. We note that for a large scale system of equations, the direct linear solver might be inefficient and costly, and iterative methods [e.g., Generalized Minimal RESidual (GMRES) [40]] can instead be used. To avoid convergence to undesirable local minima, continuations on the projection parameter (β) are considered [26]. The continuation on the projection parameter relaxes the initialized optimization problem and ensures a smooth evolution and stable convergence to satisfactory solutions. The optimization problem is considered converged if all constraints are satisfied and the relative change of the objective function is less than 10^{-6} .

5. Numerical examples

In this section, we implement the topology optimization approach in 2D, assuming plane stress state, for both biaxially and uniaxially applied strain cases. For all numerical examples, the periodic microstructured RVE given in Fig. 1c is considered, where $l_1 = l_2 = 1$. The domain is discretized with 100×100 bilinear quadrilateral elements. We note that our mesh refinement studies show

negligible discretization errors. Symmetry on the design is enforced in the axial directions and along the diagonals (Fig. 1c). To eliminate the rigid-body translation, an arbitrary node in the solid region of the design domain (shaded area in Fig. 1c) of the microscale problem is constrained in all directions and reflected based on the applied axes of symmetry. The base material parameters are set to $E = 1$ and $\nu = 0.3$. For all numerical examples, we consider continuations on the projection parameter, β . For each continuation step, sufficient inner iterations are considered to ensure a smooth evolution of the design. We consider 250 iterations for the first continuation step to encourage the initially relaxed optimization problem to converge to a stable solution. For the remaining continuation steps, β is increased every 40 optimization iterations.

5.1. Topology optimized designs

In this section, we first present topology optimization examples where we start with different initial guesses, and seek to match the target stiffness tensor, i.e., $\mathbb{C}^{\text{target}}$, at 2%, 20%, and 40% applied biaxial strain. To this end, an arbitrary geometry given in Fig. 5a is used to seed the target stiffness tensor for different applied strains. Table 2 summarizes the parameters used for the optimization problem. The minimum desirable features are set through the filter radius as given in Table 2. The resulting optimized microstructures for different applied biaxial strains are given in Fig. 6. The results reveal the influence of the initial guess on the response of the topology optimization designs. For all designs, the target stiffness tensors (given in Fig. 5b-d) are achieved within the stopping criteria of 10^{-6} for the objective, and satisfy the prescribed volume constraint. While multiple solutions (local minima) are reached, their responses are equivalent to within the stopping criterion. The evolution of the objective function is shown in the last column of Fig. 6. We note that the oscillations in the objective evolution are largely caused by the continuation in the projection parameter, β , where an update in β results in the change in the elemental density.

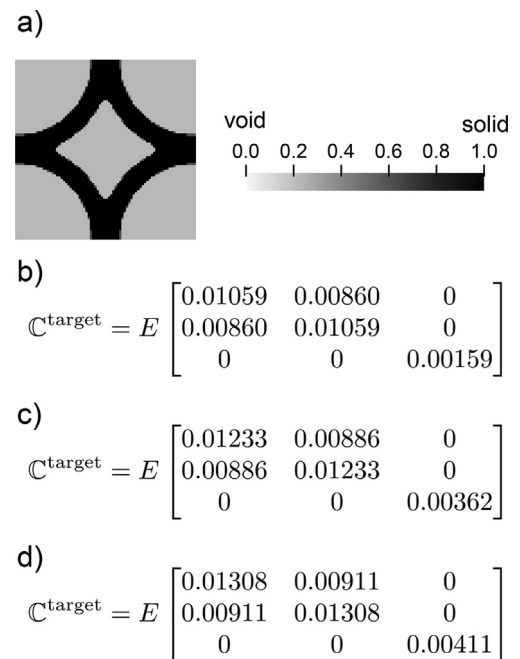


Fig. 5. a) The corresponding geometry used to seed the target stiffness tensor at b) 2%, c) 20%, and d) 40% applied biaxial strain. E is the Young's modulus of the base material.

Table 2
Topology optimization and finite element modeling parameters for the design problems.

Description	Symbol	Value
Applied biaxial macroscale strain	$\hat{E}_{xx}^M = \hat{E}_{yy}^M$	2%, 20%, 40%
Applied uniaxial macroscale strain	\hat{E}_{yy}^M	20%
Target volume fraction	V_{max}	0.305
Filter radius	r_{min}	0.0875
SIMP exponent	\bar{p}	3
Small positive number	ρ_{min}^e	10^{-4}
Threshold of the projection	η	0.50
Curvature of regularization	β	$2 \leq \beta \leq 100$

Next, we present an example undergoing uniaxial strain using this optimization framework, where two different initial guesses are considered to seek topology optimized designs that match the target stiffness tensor, i.e., \mathbb{C}^{target} , at 20% applied uniaxial strain. We note that the same arbitrary geometry given in Fig. 5a is used to seed the target stiffness tensor given in Fig. 7. All model and optimization parameters remain the same as given in Table 2. The resulting optimized microstructures are shown in Fig. 8b and Fig. 8d. Similar to previous examples, the results reveal the influence of the initial guess on the topology optimization designs' response. For both designs, the target stiffness tensor is achieved, satisfying the prescribed volume constraint. The evolution of the objective function is shown in Fig. 8e. The reported maximum discrepancy between the optimized and the

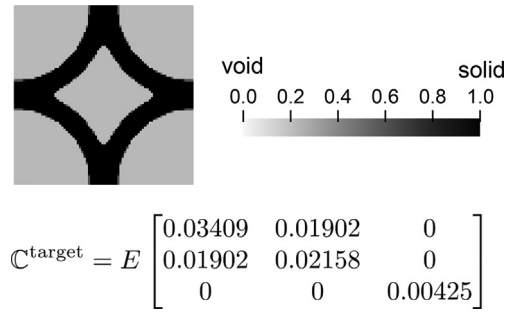


Fig. 7. The target stiffness tensor (\mathbb{C}^{target}) used in topology optimization problem under 20% uniaxial applied strain and the corresponding geometry, which was used to seed the target stiffness tensor. E is the Young's modulus of the base material.

target responses (i.e., $|\mathbb{C}_{11}^{eff} - \mathbb{C}_{11}^{target}|$) is less than 0.9%. As before, the oscillations in the objective evolution are caused by the continuation in the projection parameter, β . Again, as for the biaxial loading case, the optimized designs are not unique, and for the same target stiffness, multiple optimized designs can be obtained.

5.2. Experimental calibration

To experimentally evaluate the qualitative performance of the optimized design, the topology optimized design given in Fig. 8b

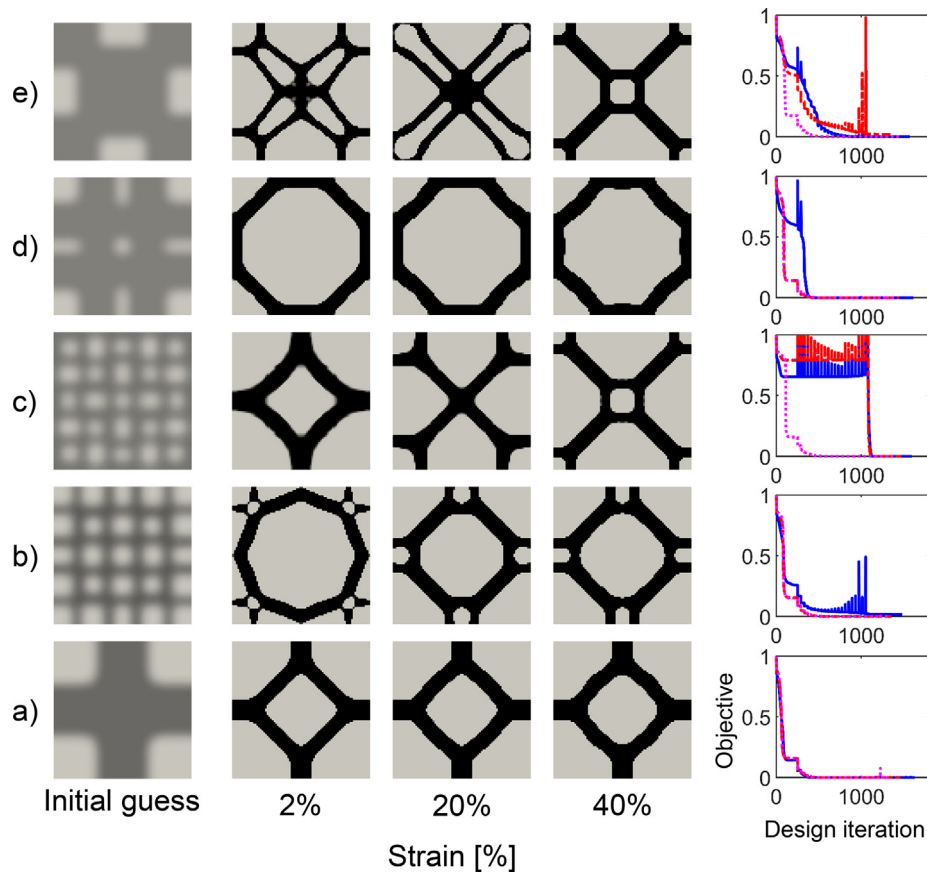


Fig. 6. Topology optimized microstructures for different initial guesses (rows a-e) under different applied biaxial strains (2%, 20%, and 40%). The evolution of the objective functions is given in the last column. The blue solid line, the red dash-dot line, and the magenta dotted line correspond to 2%, 20%, and 40% strain, respectively.

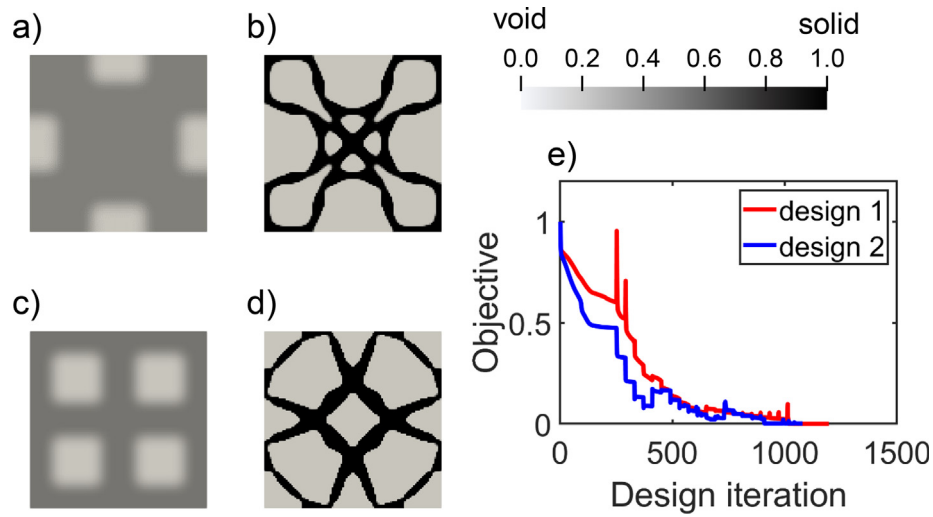


Fig. 8. Initial and optimized geometries used to, and identified that, match the target stiffness tensor at 20% uniaxial strain of the geometry shown in Fig. 7. a) Initial guess for design 1. b) Optimized design for design 1. c) Initial guess for design 2. d) Optimized design for design 2. e) The objective history for design 1 and 2.

was fabricated and tested. The samples were 3D printed using a Connex3 Objet350 printer and FLX9785 material. Each 3D printed sample was glued to acrylic plates along the top and bottom edges in order to ensure better gripping of the sample. The thickness of the printed structure was selected to be 30% of the unit cell height and width. Thicknesses significantly exceeding the characteristic length scales of the system could be expected to induce deviations from the simulated

plane stress conditions. Under the uniaxial loading condition, the mechanical testing of each sample was performed on an Instron 5965 tester. Tension tests were performed at a rate of 0.1 mm/s.

The deformed configurations of the numerical and experimental samples of the optimized geometry “design 1” (corresponding to Fig. 8b) are shown in Fig. 9a and Fig. 9f. The deformed configurations of the numerical and experimental samples corresponding to the target

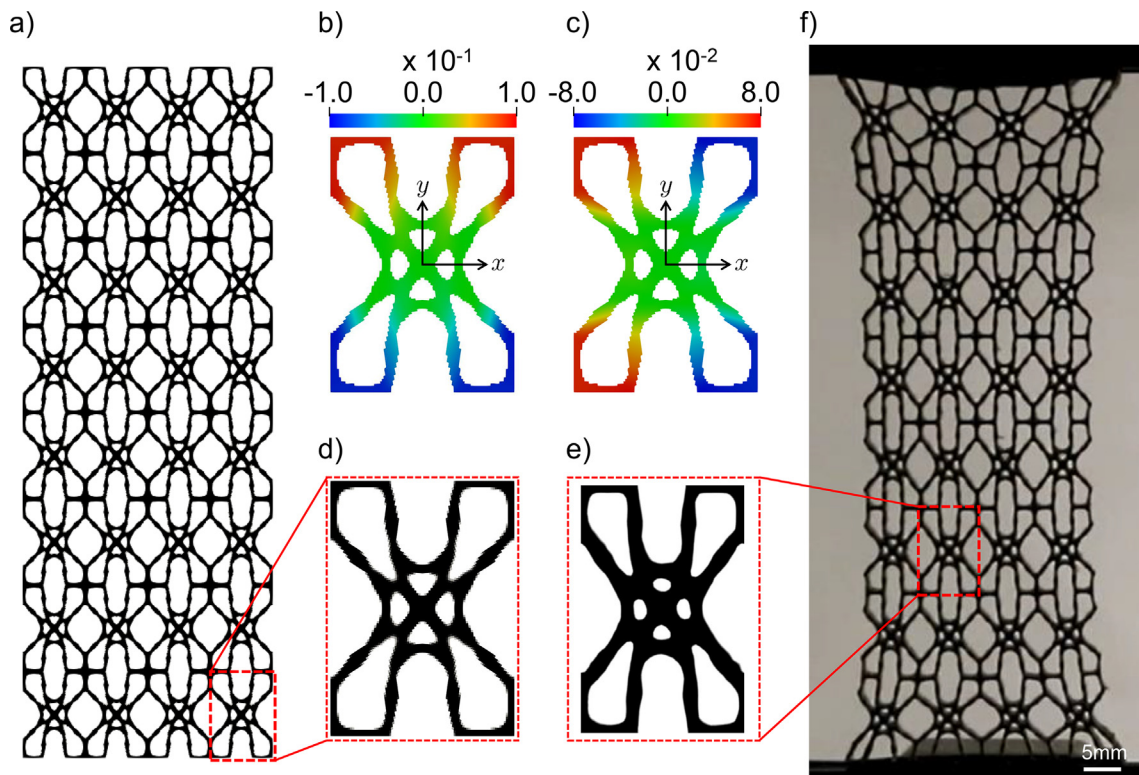


Fig. 9. The numerical and experimental deformed configurations of the optimized microstructure given in Fig. 8b at $\hat{E}_{yy}^M = 20\%$ (design 1). a) The deformed 4×8 microstructured lattice – simulation, b) displacement in y direction – simulation, c) displacement in x direction – simulation, d) the deformed RVE – simulation, e) the deformed RVE – experiment (background color removed through image processing), and f) the deformed 4×8 microstructured lattice – experiment.

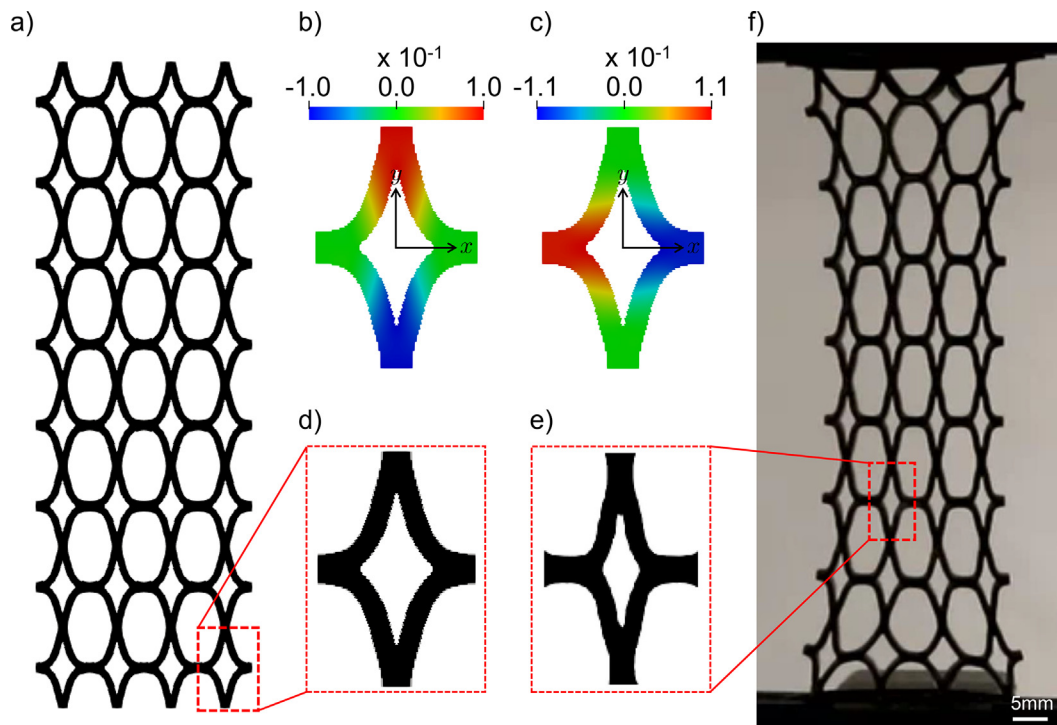


Fig. 10. The numerical and experimental deformed configurations of the target geometry at $\hat{E}_{yy}^M = 20\%$. a) The deformed 4×8 microstructured lattice – simulation, b) displacement in y direction – simulation, c) displacement in x direction – simulation, d) the deformed RVE – simulation, e) the deformed RVE – experiment (background color removed through image processing), and f) the deformed 4×8 microstructured lattice – experiment.

geometry are shown in Fig. 10a and Fig. 10f. We note that there are small discrepancies between the fabricated geometries and the optimized design, which we attribute to limited printing resolution, as well as uncertainties in pixel detection from the image processing of the experimental structure. However, the overall shape and volume fraction between the printed and optimized structures are similar. The measured volume fraction of the printed optimized design is 0.43 and the measured volume fraction of the printed target design is 0.29. The comparison of the experimental and numerical stress–strain responses is shown in Fig. 11. The experimentally measured stress–strain curves are normalized such that the maximum stress measured of the target geometry is set equal to the computed maximum stress. The results show qualitatively similar trends in the stress–strain responses. The use of elastomeric type materials, and thus nonlinear elastic material response in the experimental samples, may contribute to the discrepancy between the experimental and numerical results. The differing boundary conditions between the experiment (fixed boundaries) and simulation (periodic boundaries) may also play a significant role. In Fig. 11c, d, the normalized modulus versus strain is calculated by taking the numerical derivative of the normalized stress–strain data with respect to strain. The oscillations observed in Fig. 11c represent transitions between stiffening and softening behavior, which can be caused by geometric changes occurring under large deformation. An example of such a change is snap-through-like behavior, wherein the concavity of a microstructural element flips when a critical deformation is reached. For both designs 1 and 2, it is clear that the numerical responses cross the target response at 20% strain. For design 1, the experimental response crosses the target response close to 20% applied strain, as intended.

6. Conclusions

This paper presented a method for the design optimization of periodic microstructured materials with prescribed nonlinear constitutive properties over finite strain ranges. For the demonstrated examples, we considered only the geometric nonlinearity. An optimization problem was formulated to match a target mechanical response. This was accomplished by integrating a nonlinear homogenization technique into the formulation of a topology optimization algorithm that considers the effects of locally varying macroscopic strain/stress on the response of the microstructured unit cell. Adjoint sensitivities were derived to compute the generalized sensitivities of the homogenized tangent stiffness tensor with respect to design and state variables. Two-dimensional topology optimization examples were considered to study the performance of the presented approach. An optimized design was additively manufactured and its response was calibrated through the experiment. The topology optimization approach enables the design of nonlinear lattice-like materials with tailored homogenized constitutive properties, for applications ranging from impact mitigation to wearable electronics.

CRedit authorship contribution statement

Reza Behrou: Writing - original draft, Writing - review & editing, Methodology, Software, Investigation. **Maroun Abi Ghanem:** Writing - review & editing, Investigation. **Brianna C. Macnider:** Writing - review & editing, Investigation. **Vimarsh Verma:** Writing - review & editing, Investigation. **Ryan Alvey:** Writing - review & editing, Investigation. **Jinho Hong:** Writing - review & editing, Investigation. **Ash-**

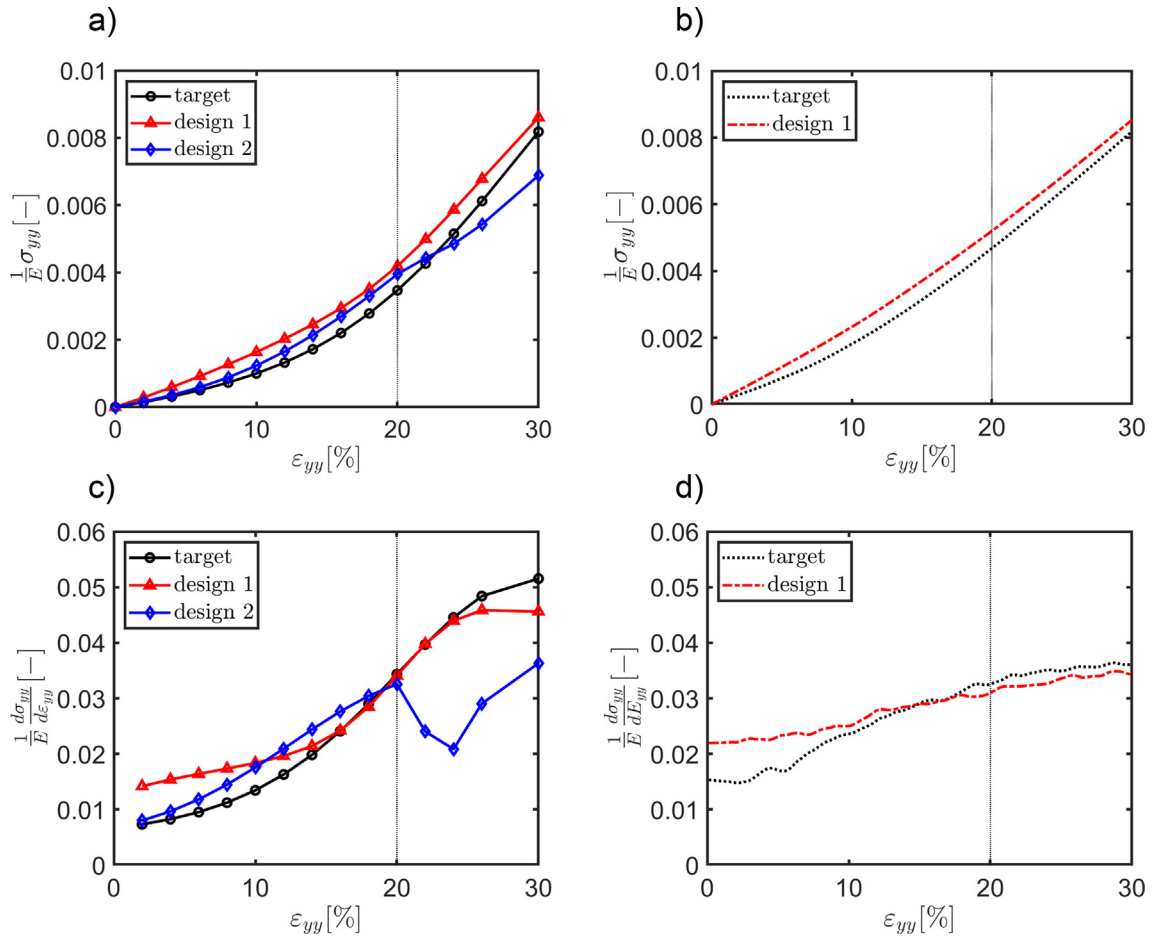


Fig. 11. a) The numerical stress–strain responses for the target geometry and optimized designs. b) The experimental stress–strain responses for the target geometry and design 1. c) The derivative of the numerical stress–strain responses with respect to the strain in loading direction (ϵ_{yy}). d) The derivative of the experimental stress–strain responses with respect to the strain in loading direction (ϵ_{yy}).

Iey F. Emery: Writing - review & editing, Supervision. **Hyunsun Ali-cia Kim:** Writing - review & editing, Supervision. **Nicholas Boechler:** Conceptualization, Writing - review & editing, Supervision.

Declaration of Competing Interest

The authors declare that they have no known competing financial interests or personal relationships that could have appeared to influence the work reported in this paper.

Acknowledgments

This work was supported by the Air Force Office of Scientific Research under award number FA9550-16-1-0142. R. B. thanks Dr. N. P. van Dijk for useful discussions on the homogenization technique.

Appendix A. Homogenization matrices

For two spatial dimensions, the nodal coordinate matrix, T_X , is defined as follows:

$$T_X = \begin{bmatrix} \vdots & \vdots & \vdots & \vdots & \vdots & \vdots \\ X_1^i & X_2^i & 0 & 0 & 0 & 0 \\ 0 & 0 & X_1^i & X_2^i & 0 & 0 \\ 0 & 0 & 0 & 0 & X_1^i & X_2^i \\ \vdots & \vdots & \vdots & \vdots & \vdots & \vdots \end{bmatrix}_{2n \times 4} \quad (A.1)$$

The following relationship is held between the symmetric displacement gradient vector, \widehat{G}_{sym}^M , the original displacement gradient, \widehat{G}^M , and the Green–Lagrange strain tensors (under the assumption of the rotation-free deformation) [20]:

$$\begin{aligned} \widehat{G}^M &= T_s \widehat{G}_{sym}^M, \\ \widehat{E}^M &= (\bar{I} + \frac{1}{2} \widehat{G}^M) \widehat{G}_{sym}^M, \end{aligned} \quad (A.2)$$

where

$$T_s = \begin{bmatrix} 1 & 0 & 0 & 0 & 0 & 0 & 0 & 0 & 0 \\ 0 & 0 & 0 & 0 & 1 & 0 & 0 & 0 & 0 \\ 0 & 0 & 0 & 0 & 0 & 0 & 0 & 0 & 1 \\ 0 & 1 & 0 & 1 & 0 & 0 & 0 & 0 & 0 \\ 0 & 0 & 0 & 0 & 0 & 1 & 0 & 1 & 0 \\ 0 & 0 & 1 & 0 & 0 & 0 & 1 & 0 & 0 \end{bmatrix}^T \quad (A.3)$$

The matrix \bar{G}^M collects the components of the symmetric displacement gradient, \widehat{G}_{sym}^M , is given as follows:

$$\bar{G}^M = \begin{bmatrix} G_{11}^M & 0 & 0 & G_{12}^M & 0 & G_{31}^M \\ 0 & G_{22}^M & 0 & G_{12}^M & G_{23}^M & 0 \\ 0 & 0 & G_{33}^M & 0 & G_{23}^M & G_{31}^M \\ G_{12}^M & G_{12}^M & 0 & (G_{11}^M + G_{22}^M) & G_{31}^M & G_{23}^M \\ 0 & G_{23}^M & G_{23}^M & G_{31}^M & (G_{22}^M + G_{33}^M) & G_{12}^M \\ G_{31}^M & 0 & G_{31}^M & G_{23}^M & G_{12}^M & (G_{33}^M + G_{11}^M) \end{bmatrix} \quad (A.4)$$

- [33] Andreassen E, Lazarov BS, Sigmund O. Design of manufacturable 3d extremal elastic microstructure. *Mech Mater* 2014;69(1):1–10.
- [34] Arora J, Wang Q. Review of formulations for structural and mechanical system optimization. *Struct Multidisc Optim* 2005;30(4):251–72.
- [35] Sigmund O, Petersson J. Numerical instabilities in topology optimization: a survey on procedures dealing with checkerboards, mesh-dependencies and local minima. *Struct Optimiz* 1998;16(1):68–75.
- [36] Guest JK, Prévost JH, Belytschko T. Achieving minimum length scale in topology optimization using nodal design variables and projection functions. *Int J Numer Meth Eng* 2004;61(2):238–54.
- [37] Sigmund O. Morphology-based black and white filters for topology optimization. *Struct Multidisc Optim* 2007;33(4–5):401–24.
- [38] Sigmund O, Maute K. Topology optimization approaches. *Struct Multidisc Optim* 2013;48(6):1031–55.
- [39] Gilbert JR, Moler C, Schreiber R. Sparse matrices in matlab: design and implementation. *SIAM J Matrix Anal Appl* 1992;13(1):333–56.
- [40] Saad Y, Schultz MH. Gmres: a generalized minimal residual algorithm for solving nonsymmetric linear systems. *SIAM J Sci Stat Comput* 1986;7(3):856–69.